Noname manuscript No.
(will be inserted by the editor)

A minimal solution for the single plane calibration of a freehand 3D ultrasound

Francisco Vasconcelos · Neide Simões · João P. Barreto

Received: date / Accepted: date

Abstract Freehand 3D ultrasound (US) refers to instrumenting a conventional US probe with a tracking device such that successive 2D scans can be registered in a stationary 3D world reference frame. The technique invariably requires a calibration procedure for finding the rotation, translation, and scaling of the scan plane with respect to the tracking device. We describe the first minimal, closed-form solution for calibrating the US probe using a single-plane phantom that is able to determine the 8 unknown degrees-of-freedom (DOF) from as little as 4 frames. This minimal solution is used in a hypothesis-and-test framework for accomplishing robust calibration in a fully automatic manner. Experiments with a low resolution curvilinear probe show that we can obtain calibrations with point reconstruction accuracy of 1.06 mm for scans up to 120 mm depth using as little as 30 frames. Our method reaches state-of-the-art metric accuracy with a much smaller number of input frames when comparing to other calibration methods.

Keywords Ultrasound · Geometric calibration

1 Introduction

Freehand 3D ultrasound (US) [6] is a technique where a hand-held 2D US is instrumented with a 3D tracking device such that successive scans can be registered in a common world coordinate system. The technique has applications in different clinical domains including 3D reconstruction during US examination [6,8], 3D registration of organs in computer-aided surgery [28,18], and orientation of needles (probes) during US guided biopsy [27]. In particular, the dissemination of interventional imaging is contributing for the increasingly popularity of freehand 3D US among clinicians, with several manufacturers providing the required equipment (e.g. BrainLab, SonoWand).

The technique consists in freely moving a standard 2D US probe while a pose tracking system measures its 3D rotation and translation such that pixel coordinates in each 2D US scan are mapped into 3D metric coordinates in a stationary reference frame (the world coordinate system). Pose tracking can be accomplished with different technologies such as optical [18,33], electromagnetic [14], mechanical [32], or cameras operating in the visible spectrum [27]. These technologies require the 2D US probe to be instrumented with a tracking sensor or device whose reference frame is not coincident with the system of coordinates of the US image. Thus, representing the US depth readings in world coordinates invariably passes by determining the transformation that maps 2D image pixels in the US scans into 3D points in the reference frame of the tracking sensor [20] (Fig. 1). This is accomplished through a preliminary calibration procedure that estimates the 8 unknown Degrees-of-Freedom (DOFs): 3 for rotation, 3 for translation, and 2 for the XY scale of the US scan.

The calibration is typically carried using a phantom object that is registered in the coordinate system of the tracking sensor. The depth of certain phantom features (e.g. points, lines, etc) are measured by the US probe in different positions until there are enough geometric

F. Vasconcelos performed this research while affiliated to Institute for Systems and Robotics, University of Coimbra, Portugal.
and is currently affiliated with
Wellcome / EPSRC Interventional and Surgical Sciences (WEISS), University College London, United Kingdom.
N. Simões, J. P. Barreto
Institute for Systems and Robotics, University of Coimbra, Portugal.
E-mail: f.vasconcelos@ucl.ac.uk

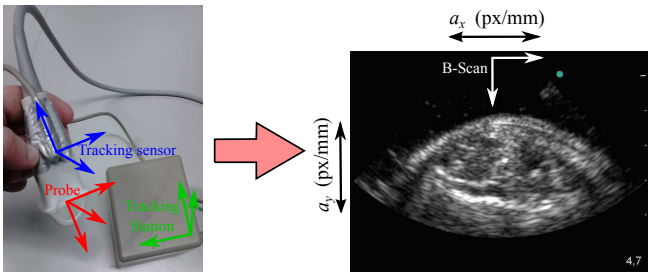

Fig. 1 Overview of a freehand 3D US system. A freely moving US probe is tracked in real time by a rigidly attached sensor. In this figure the marker is an electromagnetic sensor whose pose is determined by a tracking station. This enables to map 3D objects to image coordinates of US scans.

constraints to accurately determine the mapping transformation. The phantom is either immersed in water or in a gel with similar acoustic properties to human tissue. The procedure is usually time consuming because it requires to carefully collect a large number of input frames, as well as pin-pointing features in the 2D US scans to establish correspondences. The poor usability of existing methods preclude the calibration to be carried in the Operating-Room (OR) right before starting each procedure, with most commercial equipments having a rigid configuration that is set-up from factory.

This article describes a new fast, robust, and fully automatic calibration method that can be used in OR by a non-expert user with benefits in terms of accuracy, flexibility, and cost. First, the fact that the calibration is carried before each usage prevents deviation in factory pre-sets along time that affect metric accuracy. Second, the clinician is no longer limited to a particular equipment set-up having the freedom to choose the US probe, the image tunings, and the place where to attach the tracking device depending on what is better suited for the clinical procedure to be carried. And third, the easy calibration enables to combine different tracking systems with already existing US equipments as opposed to purchasing a new integrated solution.

The literature reports a large number of possible phantoms from which the simplest and cheapest is a single plane surface. Our method uses a single plane whose 3D pose is known in the coordinate frame of the tracking system. The technical contributions of the paper are as follows:

- *Minimal solution for single-plane calibration:* The unknown transformation has 8 DOFs and each scan provides 2 independent constrains, which means that in theory the calibration problem can be solved using a minimum of 4 images. The article describes a minimal solution for this problem that, given 4 scans of the phantom plane, it computes 2 possible solutions for the transformation between US and tracking sensor. This is accomplished by extending the minimal algorithm in [30] to also compute the XY scale of the US image.
- *Pipeline for unsupervised, robust calibration:* Since the phantom is a plane, the features to be detected in the US scans are continuous lines. In order to avoid the need of human intervention the line features are automatically detected, which raises issues of robustness and accuracy because of the risk of mis-detection and/or poor estimation of line position. This difficulty is overcome by using the minimal algorithm in an iterative Random Sampling Consensus (RANSAC) step to discard outlier inputs [7]. The final result is a complete calibration pipeline that is fully automatic and robust. Computational efficiency is assured by the minimal solution that reduces the combinatorics of the RANSAC robust estimator.
- *High accuracy with small number of input frames:* Extensive experiments with a visually tracked curvilinear probe in realistic calibration conditions show good repeatability of results using 10 or more input frames. For an imaging depth up to 130mm the average Point Reconstruction Accuracy (PRA) is 2.2mm and 1.0mm for 10 and 30 calibration images, respectively. These accuracies compare with the current state-of-the-art method [22] that reports a PRA of 1.0mm for 50 or more calibration frames. However, since we use a 2D US probe with less than half the resolution of [22], our results suggest that our method accomplishes similar accuracies with 4 to 5 times less frames.

2 Related Work

During the years literature has introduced 2D US freehand calibration methods using a wide variety of different phantoms [12]. Some methods use as a calibration target a set of 3D points at known locations. This can be achieved with spherical objects [2], sets of intersecting wires [15], or the tip of an instrumented stylus [34]. The accuracy of these methods highly depends operator's ability to precisely align the US scanning plane with the phantom target points, and the careful acquisition of calibration measurements can be extremelly time consuming. Line-based methods can use a set of wires [4] (typically in a z-shape format), a hollow tube [1], or an instrumented stylus/needle [31]. In this case a set of 3D lines with known coordinates is registered against their corresponding 2D US point sections under different views. Plane-based methods [24,25,22] use a planar surface as phantom object that is measured as

a line by the US probe. This approach can also be extended to a phantom containing multiple planes [21], increasing the number of geometric constraints per US image acquisition. Both the line-based and the plane-based approaches are more flexible than the point-based ones because any arbitrary section of a 3D line or plane can be acquired. This also makes it easier to acquire calibration images within a wider range of motions, which yields more accurate calibration results. Additionally, there are self-calibration methods that use an arbitrary unknown target volume, however these require either the US probe to be moved in a controlled way [3], or exhaustive sweeps of volumes with very distinctive visual landmarks such as the human brain [29].

Using the single plane method is specially attractive for two reasons: it uses the easiest and least expensive phantom to build; the phantom is measured in US scans as a continuous line instead of a discrete set of points, which makes it significantly more feasible to perform automatic and robust segmentation of the phantom features. Unfortunately, it suffers from the so called beam thickness problem [24]. As any other calibration approach, the single plane method requires the user to scan the phantom under a wide variety of poses, and when the US probe is oriented obliquely to the plane it produces a systematic error in line measurements. One possibility to counter this effect is to scan the phantom in symmetrical poses with respect to the plane normal, producing measurement pairs with opposite errors that cancel each other. This, however, requires the calibration process to be done in a very carefully and time consuming manner. Another approach uses the Cambridge phantom [24] to minimize the thickness beam effect but this requires a complex instrument and also makes the calibration procedure more difficult and time consuming. The older single plane methods [24,17,25, 11] use iterative minimization of re-projection errors and require hundreds of images to converge. Najafi et. al. [22] proposed a method that is able to achieve an accurate calibration using a significantly lower number of images. This is accomplished by reducing the number of unknown variables (the plane phantom coordinates are pre-determined) and by using a closed-form solution.

In this paper we aim at improving on [22] by providing a minimal closed form solution to the single plane calibration problem. The method in [31] provides a minimal solution that could be used for plane-based calibration, however, since it is formulated as a similarity registration problem, it only estimates a single US scale parameter and thus it is not suitable to US probes with different horizontal and vertical scaling parameters. Recent research in computer vision has proven the importance of the so-called minimal solutions [23,26,16], i. e. solving a problem with the same number of constraints as the number of unknowns. Minimal solutions can be efficiently used within a RANSAC framework [7] in order to produce robust estimations in the presence of outlier measurements. Rousseau et. al. [25] also use RANSAC to robustly segment lines independently in each US scan, however, since their calibration method is iterative it cannot be used within a more comprehensive RANSAC that ensures geometric consistency in all measurements simultaneously.

In the single plane calibration problem there are 8 unknowns (3 in translation, 3 in rotation, and 2 image scale factors) while each line scan provides 2 constraints. This means that the problem can be solved from a minimum of 4 line scans. Such minimal solution combined with RANSAC can overcome both the accuracy and usability limitations of single plane methods because the user can carelessly collect data while wrong acquisitions are discarded. The solution of [22] is non-minimal in the sense that it requires at least 5 line scans, and furthermore it assumes that one of the image scale parameters is known, which might not be viable with some US probes. In practice they only report results with 20 scans or more. To the best of our knowledge we propose the first minimal solution for this problem. Experiments with a low resolution curvilinear probe show that we can obtain calibrations with point reconstruction accuracy of 1.06 ± 0.53 mm for scans up to 120 mm depth using as little as 30 frames, which dramatically outperforms state-of-the-art methods.

2.1 Notation

Scalars are represented by plain letters, e.g. λ, vectors by bold symbols, e.g. $\mathbf{t}$, matrices by letters in sans serif font, e.g. T. The operator $[]_\times$ designates a 3×3 skew symmetric matrix, such that $[\mathbf{x}]_\times \mathbf{v} = \mathbf{x} \times \mathbf{v}$ for any 3×1 vectors $\mathbf{x}$, $\mathbf{v}$. The operator $\otimes$ designates the Kronecker product.

We use a letter with prime symbol, e. g. $\mathbf{\Sigma}'$, for geometric entities represented in the reference frame of the US probe. Plain letters, e. g. $\mathbf{\Pi}_i$, are used to designate geometric entities in the reference frame of the marker sensor attached to the US probe. An asterisk, e. g. $\mathbf{\Pi}_i^*$ denotes geometric entities in the reference frame of the pose tracking station. Note that the same letter with/without these additional symbols, e. g. $\mathbf{\Sigma}^*$, $\mathbf{\Sigma}'$, $\mathbf{\Sigma}$ represents the **same** geometric entity under the different reference frames.

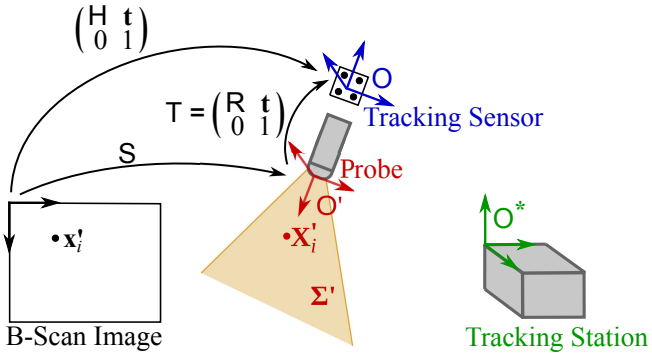

Fig. 2 Freehand 3D US model. A 2D image point $\mathbf{x}'_i$ is mapped to a 3D point $\mathbf{X}'_i$ in the probe reference frame with a scaling transformation S. Consequently, this point can be mapped to the tracking sensor reference frame through a rigid transformation T.

3 Model for the freehand 3D US

The model for the freehand 3D US is summarized in Fig. 3. A 2D US probe with reference frame O' is attached to a tracking sensor with reference frame O that is tracked by a static station with reference frame O^*. A point $\mathbf{x}'_i$ in pixel coordinates from a US scan is scaled to metric coordinates $\mathbf{X}_i$ in the US reference frame O' using the transformation

$$\mathbf{X}'_i = \mathsf{S}\mathbf{x}'_i \tag{1}$$

with

$$\mathsf{S} = \begin{pmatrix} a_x & 0 \\ 0 & a_y \\ 0 & 0 \end{pmatrix}, \quad a_x > 0, a_y > 0. \tag{2}$$

where a_x, a_y are positive scalars that convert from pixels to metric coordinates (mm). Note that, without loss of generality, we consider that points $\mathbf{X}'_i$ lie in the plane $z = 0$ in US metric coordinates O'. These points are mapped to marker coordinates O through a rigid transformation T

$$\begin{pmatrix} \mathbf{X}_i \\ 1 \end{pmatrix} = \underbrace{\begin{pmatrix} \mathsf{R} & \mathbf{t} \\ 0 & 1 \end{pmatrix}}_{\mathsf{T}} \begin{pmatrix} \mathsf{S}\mathbf{x}'_i \\ 1 \end{pmatrix}. \tag{3}$$

Since the tracking sensor pose is known in each measurement, successive scans can be registered in a static reference frame O^* to obtain a 3D US representation.

Our calibration problem consists in determining the rotation R, the translation $\mathbf{t}$, and the scaling transformation S. Note that these unknowns have 8 degrees of freedom: 3 in rotation, 3 in translation and 2 scale parameters. The complete transformation from image pixels to tracking sensor coordinates O can be condensed into a single transformation

$$\begin{pmatrix} \mathbf{X}_i \\ 1 \end{pmatrix} = \begin{pmatrix} \mathsf{H} & \mathbf{t} \\ 0 & 1 \end{pmatrix} \begin{pmatrix} \mathbf{x}'_i \\ 1 \end{pmatrix} \tag{4}$$

with

$$\mathsf{H} = \begin{pmatrix} \mathbf{h}_1 & \mathbf{h}_2 \end{pmatrix} = \begin{pmatrix} a_x\mathbf{r}_1 & a_y\mathbf{r}_2 \end{pmatrix} \tag{5}$$

where $\mathbf{h}_1$, $\mathbf{h}_2$ are the first and second columns of H, and $\mathbf{r}_1$, $\mathbf{r}_2$ are the first and second columns of R.

Note that since $||\mathbf{r}_1|| = ||\mathbf{r}_2|| = 1$, both S and R can be easily extracted from H and thus determining $\mathbf{h}_1, \mathbf{h}_2, \mathbf{t}$ solves the calibration problem. Additionally, since R is an orthogonal matrix the following quadratic constraint must be verified

$$\mathbf{a}_1{}^{\mathsf{T}}\mathbf{a}_2 = 0 \tag{6}$$

This calibration problem can be solved with at least 8 constraints on the parameters $\mathbf{h}_1, \mathbf{h}_2, \mathbf{t}$.

4 Single Plane Calibration

The single plane method requires a planar phantom object that is registered in the coordinate system of the tracking sensor. The calibration procedure is displayed in Fig. 4 and consists in acquiring a set of US scans with the US probe under significantly different poses. The US probe measures a line $\mathbf{L}'_i$ that belongs to the phantom plane $\mathbf{\Pi}_i$. For each line measurement the phantom plane is obtained in the tracking sensor reference frame O as

$$\mathbf{\Pi}_i = \mathsf{M}_i{}^{-\mathsf{T}}\mathbf{\Pi}^* \tag{7}$$

where M_i is the rigid transformation from the tracking sensor to the tracking station, and $\mathbf{\Pi}^*$ is the calibration plane in the tracking sensor reference frame O. M_i is a different sensor measurement in each acquisition and $\mathbf{\Pi}^*$ is a fixed plane that is pre-determined before the calibration procedure.

4.1 Minimal Solution with known S

We start by formulating our calibration problem for an easier scenario in which the scale factors s_x and s_y are known. In this case the problem is identical to the extrinsic calibration between a camera and a laser rangefinder using a planar checkerboard, which in [30] it was shown to be equivalent to the Perspective-3-Point (P3P) problem [9]. In this section we provide a simpler derivation of the same result and describe how it can be applied to freehand 3D US calibration.

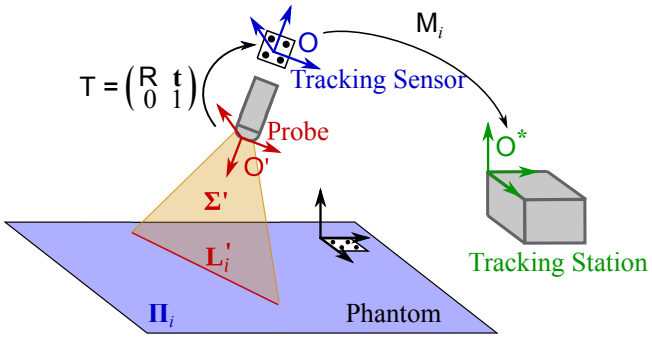

Fig. 3 Calibration set-up with planar phantom. The US probe measures a line cut $\mathbf{L}_i$, while the phantom plane is simultaneously determined in the tracking sensor reference frame O through the tracking station. The transformation T_P is pre-determined, while $\mathsf{T}_{M,i}$ is measured in each acquisition.

For each acquisition with the US probe we obtain a line $\mathbf{l}'_i$ in pixel coordinates and a plane $\mathbf{\Pi}_i$ represented in O. In this case, the lines $\mathbf{l}'_i$ can be readily scaled to metric coordinates $\mathbf{L}'_i$ and the calibration problem becomes the 3D euclidean alignment between a set of planes $\mathbf{\Pi}_i$ in the tracking sensor reference frame O and a set of co-planar lines $\mathbf{L}'_i$ that lie in the US measuring plane $\mathbf{\Sigma}'$ (Fig. 4(a)). This problem has already been solved for a minimum of 3 line measurements in the context of extrinsic calibration between a camera and a laser rangefinder [30], and we now review this method.

Consider Fig. 4(b), that represents 3 line measurements $\mathbf{L}'_1, \mathbf{L}'_2, \mathbf{L}'_3$ in the US cutting plane $\mathbf{\Sigma}'$. In general, each pair of lines $\mathbf{L}'_i, \mathbf{L}'_j$ intersects at a point $\mathbf{P}'_{ij}$. Now consider the planes $\mathbf{\Pi}_1, \mathbf{\Pi}_2, \mathbf{\Pi}_3$ represented in O. Each plane $\mathbf{\Pi}_i$ contains its correspondent US line $\mathbf{L}'_i$ (represented in blue in Fig. 4(c)). In general, each pair of planes $\mathbf{\Pi}_i, \mathbf{\Pi}_j$ intersects at a line with direction $\mathbf{d}_{ij}$ that goes through the corresponding point $\mathbf{P}'_{ij}$. The 3 planes also intersect at a single point $\mathbf{M}$. Note that the points $\mathbf{P}'_{ij}$, the point $\mathbf{M}$, and the directions $\mathbf{d}_{ij}$ can be easily determined from measurement data by intersecting the known lines $\mathbf{L}'_i$ and the known planes $\mathbf{\Pi}_i$.

From Fig. 4(c) it can be observed that points $\mathbf{P}'_{ij}$ are represented in O as

$$\mathbf{P}_{ij} = \mathsf{R}\mathbf{P}'_{ij} + \mathbf{t} \tag{8}$$

which leads to the following equation

$$\mathsf{R}\mathbf{P}'_{ij} + \mathbf{t} = \mathbf{M} + \alpha_{ij}\mathbf{d}_{ij} \tag{9}$$

where α_{ij} is the unknown depth from $\mathbf{M}$ to $\mathbf{P}_{ij}$. Determining the 3 depths α_{12}, α_{13}, α_{23} is known as the *p3p* problem, which leads to the following system of equations:

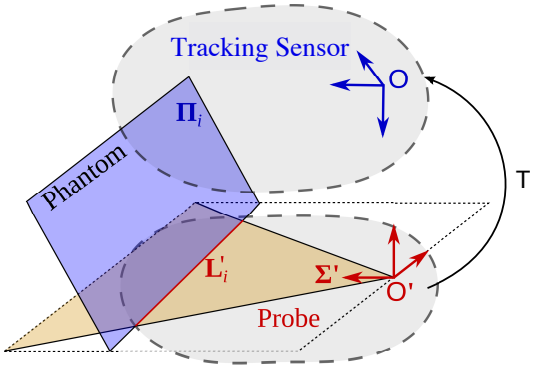

(a) For each line $\mathbf{L}'_i$ measured by the US probe corresponds a plane $\mathbf{\Pi}_i$ in the tracking sensor reference frame.

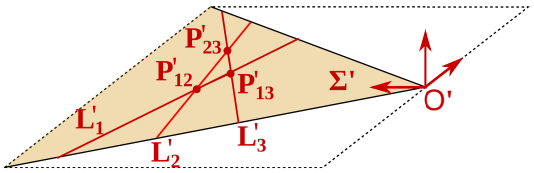

(b) For 3 plane-line measurements, each pair of lines $\mathbf{L}'_i, \mathbf{L}'_j$ intersects at point $\mathbf{P}'_{ij}$.

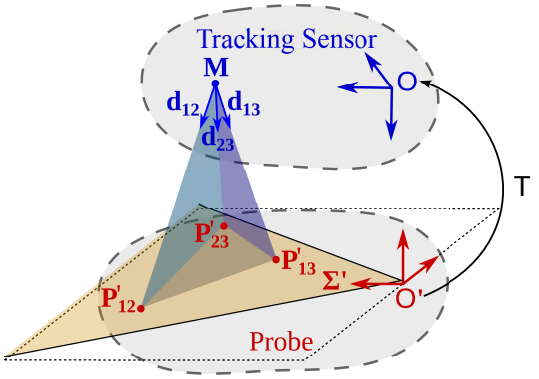

(c) Each pair of planes $\mathbf{\Pi}'_i, \mathbf{\Pi}'_j$ intersects at line with direction $\mathbf{d}_{ij}$; the three planes intersect at point $\mathbf{M}$; the classic *p3p* problem emerges from the 3 orientations $\mathbf{d}_{ij}$ and their corresponding 3D points $\mathbf{P}'_{ij}$.

Fig. 4 From registration of planes and co-planar lines to the *p3p* problem.

$$\begin{cases} \alpha_{12}^2 + \alpha_{13}^2 - \alpha_{12}\alpha_{12}\mathbf{d}_{12}{}^\top\mathbf{d}_{13} = ||\mathbf{P}'_{12} - \mathbf{P}'_{13}||^2 \\ \alpha_{12}^2 + \alpha_{23}^2 - \alpha_{12}\alpha_{12}\mathbf{d}_{12}{}^\top\mathbf{d}_{23} = ||\mathbf{P}'_{12} - \mathbf{P}'_{23}||^2 \\ \alpha_{13}^2 + \alpha_{23}^2 - \alpha_{12}\alpha_{12}\mathbf{d}_{13}{}^\top\mathbf{d}_{23} = ||\mathbf{P}'_{13} - \mathbf{P}'_{23}||^2 \end{cases} . \tag{10}$$

Multiple methods are available in the literature to solve this system [9], which has up to 8 solutions. Once depths α_{ij} are known it is possible to obtain the 3 points $\mathbf{P}_{ij} = \mathbf{M} + \alpha_{ij}\mathbf{d}_{ij}$. The rotation R and translation $\mathbf{t}$ are determined by substituting points $\mathbf{P}_{ij}$, $\mathbf{P}'_{ij}$ in 3 instances of equation 8. This is known as the *Absolute Orientation* problem, for which a solution is also available in the literature [10].

We now summarize the complete algorithm for estimating the minimal solution for the rotation R and translation $\mathbf{t}$ using 3 line measurements $\mathbf{L}'_1$, $\mathbf{L}'_2$, $\mathbf{L}'_3$ and the corresponding planes $\mathbf{\Pi}_1$, $\mathbf{\Pi}_2$, $\mathbf{\Pi}_3$.

Algorithm 1 Minimal solution with known S

1. For each two planes $\mathbf{\Pi}_i$, $\mathbf{\Pi}_j$ determine the direction $\mathbf{d}_{ij}$ of their intersecting line, by cross-multiplying the plane normals.
2. Determine the point intersection $\mathbf{M}$ of the planes $\mathbf{\Pi}_1$, $\mathbf{\Pi}_2$, $\mathbf{\Pi}_3$. This can be done by computing the null space of $\begin{pmatrix}\mathbf{\Pi}_1 & \mathbf{\Pi}_2 & \mathbf{\Pi}_3\end{pmatrix}$.
3. For each two lines $\mathbf{L}'_i$, $\mathbf{L}'_j$ determine their point intersection $\mathbf{P}'_{ij}$.
4. Formulate the *p3p* problem by substituting $\mathbf{P}'_{ij}$ and $\mathbf{d}_{ij}$ in equation 10. Obtain 3 depths α_{ij} using any standard *p3p* approach [9]. There are up to 8 different solutions.
5. Determine 3 points $\mathbf{P}_{ij} = \mathbf{M} + \alpha_{ij}\mathbf{d}_{ij}$.
6. Formulate the *Absolute Orientation* problem by substituting points $\mathbf{P}_{ij}$ and $\mathbf{P}'_{ij}$ in equation 8. Obtain the rotation R and the translation $\mathbf{t}$ using a standard *Absolute Orientation* approach [10].

This problem has up to 8 discrete solutions for 3 plane-line measurements $(\mathbf{\Pi}_i, \mathbf{L}'_i)$. When 4 or more plane-line measurements are available, a single solution can be obtained by combining the minimal solution with RANSAC [7]. We describe this method later in this paper.

4.2 Minimal Solution for the general case

In general S is not known which means that in relation to the previous case we have 2 more unknowns and an additional plane-line measurement is required. In this case the 4 lines $\mathbf{L}'_i$ and the intersection points $\mathbf{P}'_{ij}$ cannot be readily determined. Each pair of 2D lines $\mathbf{l}'_i$, $\mathbf{l}'_j$ in pixel coordinates intersects at a point $\mathbf{p}'_{ij}$ (Fig. 5(a)), such that

$$\mathbf{P}'_{ij} = \mathsf{S}\mathbf{p}'_{ij} \tag{11}$$

When there are 4 plane-line correspondences, in general each of the 6 pairs of lines $\mathbf{L}'_i$, $\mathbf{L}'_j$ intersects at a point $\mathbf{P}'_{ij}$. Additionally, each of the 6 pairs of planes $\mathbf{\Pi}_i$, $\mathbf{\Pi}_j$ intersects at a line with direction $\mathbf{d}_{ij}$ and each of the 4 triplet of planes $\mathbf{\Pi}_i$, $\mathbf{\Pi}_j$, $\mathbf{\Pi}_k$ intersects at a point $\mathbf{M}_{ijk}$. In Fig. 5(b) we display the intersections for a triplet of planes $\mathbf{\Pi}_1$, $\mathbf{\Pi}_2$, $\mathbf{\Pi}_3$.

Substituting points $\mathbf{p}'_{ij}$ in equation 9 yelds

$$\mathsf{H}\mathbf{p}'_{ij} + \mathbf{t} = \mathbf{M}_{ijk} + \alpha_{ij}\mathbf{d}_{ij} \tag{12}$$

The unknown scalars α_{ij} can be eliminated using cross product

$$[\mathbf{d}_{ij}]_\times \mathsf{H}\mathbf{p}'_{ij} + [\mathbf{d}_{ij}]_\times \mathbf{t} = [\mathbf{d}_{ij}]_\times \mathbf{M}_{ijk} \tag{13}$$

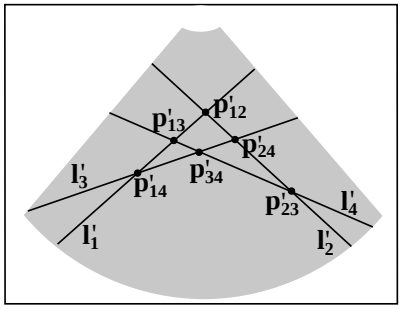

(a) 4 lines $\mathbf{l}'_i$ on the US image intersect at six 2D points $\mathbf{p}'_{ij}$.

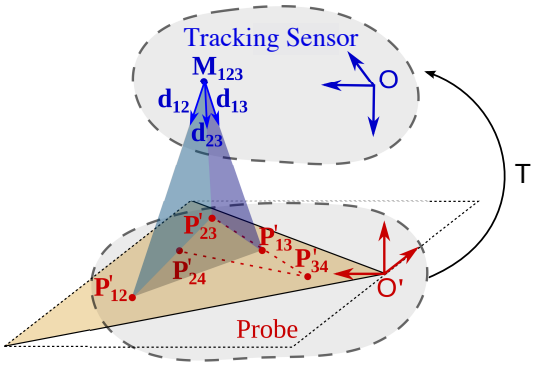

(b) Each of the 4 triplets of planes $\mathbf{\Pi}_i$, $\mathbf{\Pi}_j$, $\mathbf{\Pi}_k$ intersects at a point $\mathbf{M}_{ijk}$ and the directions $\mathbf{d}_{ij}$, $\mathbf{d}_{ik}$, $\mathbf{d}_{jk}$ that are aligned with the points $\mathbf{P}'_{ij}$, $\mathbf{P}'_{ik}$, $\mathbf{P}'_{jk}$.

Fig. 5 Registration of 4 Line-plane correspondences.

Finally this equation can be re-written as

$$\left(\mathbf{p}'_{ij} \otimes [\mathbf{d}_{ij}]_\times \; [\mathbf{d}_{ij}]_\times\right) \left(\mathbf{a}_1{}^\mathsf{T} \; \mathbf{a}_2{}^\mathsf{T} \; \mathbf{t}^\mathsf{T}\right)^\mathsf{T} = [\mathbf{d}_{ij}]_\times \mathbf{M}_{ijk} \tag{14}$$

Each instance of equation 14 puts 2 linear constraints on the 9 parameters of $\mathbf{a}_1$, $\mathbf{a}_2$, $\mathbf{t}$. Although all combinations of line and point intersections provide 12 instances of equation 14, there are only 8 linearly independent constraints of this form. Stacking these 8 relations generates a linear system in 9 variables that can be solved up to an unknown parameter β. Equation 6 is then used to determine β and find the parameters $\mathbf{a}_1$, $\mathbf{a}_2$, $\mathbf{t}$.

We now summarize our minimal algorithm step by step. Consider 4 correspondences between planes $\mathbf{\Pi}_i$ in the visual tracking sensor reference frame and 4 lines $\mathbf{l}'_i$ in US image coordinates.

This problem has up to 2 discrete solutions for 4 plane-line measurements $(\mathbf{\Pi}_i, \mathbf{L}'_i)$. Analogously to the previous simpler case, when 5 or more plane-line measurements are available, a single solution can be obtained by combining the minimal solution with RANSAC.

Algorithm 2 Minimal solution with unknown S

1. Determine the line direction $\mathbf{d}_{ij}$ for the intersection of each pair of planes $\mathbf{\Pi}_i$, $\mathbf{\Pi}_j$.
2. Determine the point intersection $\mathbf{M}_{ijk}$ for each triplet of planes $\mathbf{\Pi}_i$, $\mathbf{\Pi}_j$, $\mathbf{\Pi}_k$.
3. Determine the point intersection $\mathbf{p}'_{ij}$ for each pair of lines $\mathbf{l}'_i$, $\mathbf{l}'_j$.
4. Substitute $\mathbf{d}_{ij}$, $\mathbf{M}_{ijk}$, $\mathbf{p}'_{ij}$ in equation 14 until 8 linearly independent equations are found.
5. Solve the linear system up to one scalar unknown β, such that $\mathsf{A} = \beta\mathsf{A}_1 + \mathsf{A}_2$ and $\mathbf{t} = \beta\mathbf{t}_1 + \mathbf{t}_2$.
6. Substitute $\beta\mathsf{A}_1 + \mathsf{A}_2$ in equation 6 to determine β. There are up to 2 solutions.
7. For each $(\mathbf{a}_1, \mathbf{a}_2, \mathbf{t})$ solution, find the positive values a_x, a_y such that $\mathbf{r}_1$,$\mathbf{r}_2$ from equation 5 have unitary norm.
8. Determine the rotation as $\mathsf{R} = \begin{pmatrix}\mathbf{r}_1 & \mathbf{r}_2 & \mathbf{r}_1 \times \mathbf{r}_2\end{pmatrix}$

4.3 Degenerate Configurations

We now discuss the degenerate configurations of the general calibration problem for which the solutions for R, $\mathbf{t}$, S are ambiguous. This helps to understand how the US probe should be positioned in different acquisitions to avoid inaccurate calibration results.

When all lines $\mathbf{L}'_i$ are parallel there is a translational ambiguity along the same direction (Fig. 6(a)). In our calibration problem we are in this configuration when all acquisitions are done by moving the probe without rotation, or just with rotations that are either around the $x-$axis of O' or around an axis perpendicular to the phantom plane. When all the line directions $\mathbf{d}_{ij}$ are parallel, there is a translational ambiguity along the same direction (Fig. 6(b)). This happens in our problem when all planes $\mathbf{\Pi}_i$ have co-planar normals, i. e., all acquisitions are done by rotating the probe along an axis parallel to the calibration plane. Finally, when all points $\mathbf{M}_{ijk}$ are coincident, there is a scale factor ambiguity (Fig. 6(c)). In this case we can always scale a_x,a_y in order to put the probe further away or closer to the calibration plane. This situation occurs when all acquisitions are done by rotating the probe around a single point on the phantom plane.

To summarize, degenerate configurations can be avoided by measuring different regions of the calibration plane and by exploring all three degrees of freedom in rotation when moving the probe between different acquisitions.

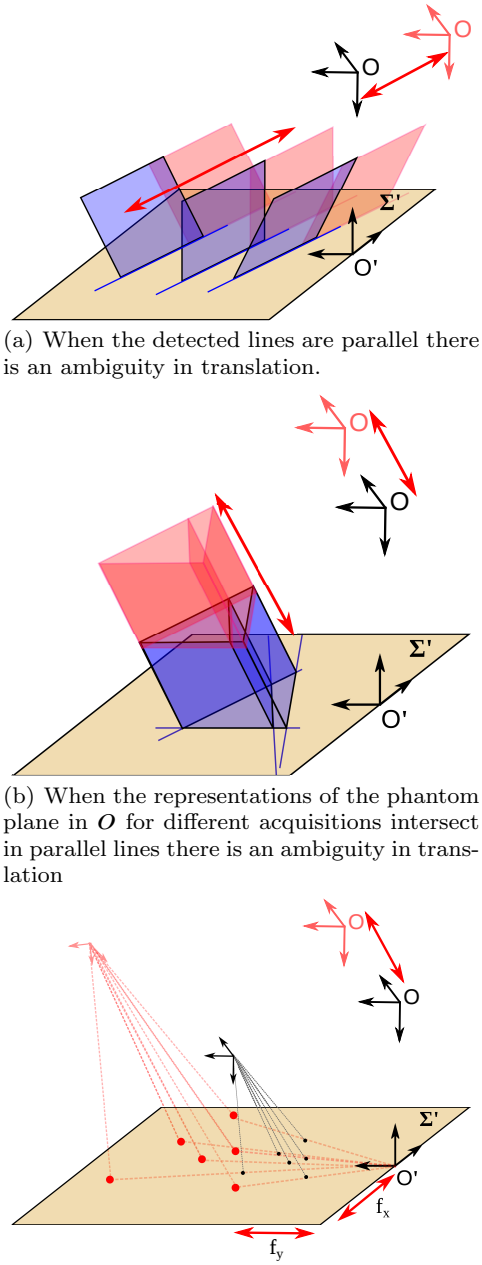

(a) When the detected lines are parallel there is an ambiguity in translation.

(b) When the representations of the phantom plane in $\boldsymbol{O}$ for different acquisitions intersect in parallel lines there is an ambiguity in translation

(c) When the representations of the phantom plane in $\boldsymbol{O}$ for different acquisitions intersect at the same point there is an ambiguity in scale and translation.

Fig. 6 Degenerate configurations.

5 Practical Considerations

5.1 Automatic Line Detection

We perform automatic line segmentation on the US scan images using the Hough transform [5]. However, artifacts caused by undesired reflections may produce multiple line detections (Fig. 7(a)). While it might be easy for a human observer to select which line corresponds to the phantom plane, performing this selection automatically is not trivial, given that the maximum Hough peak does not always correspond to the correct line. In order to deal with this problem we use the PEARL approach for multi-model fitting [13] to remove spurious line detections, while still considering multiple line segment candidates in ambiguous cases.

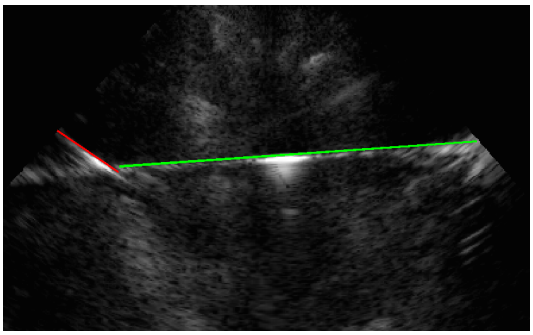

(a) The green line segment is a correct detection of the calibration plane while the red is an incorrect detection produced by an undesired artifact on the US image.

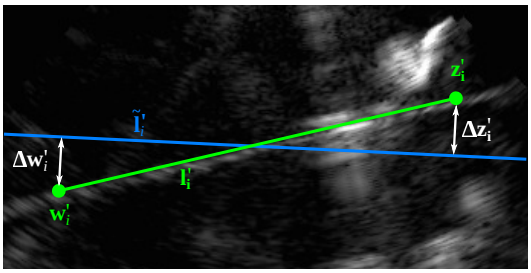

(b) Line segment detections are represented by start and end points $\mathbf{w}'_{i,j}$, $\mathbf{z}'_{i,j}$. RANSAC uses as error metric the orthogonal distances between these points and the re-projected line $\tilde{\mathbf{l}}'_{i,j}$.

Fig. 7 Line detection with Hough transform and PEARL.

For each scan PEARL detects line segments defined by their start and end points $\mathbf{w}'_{i,j}$, $\mathbf{z}'_{i,j}$ (Fig. 7(b)). Each line candidate, even if belonging to the same image, is considered as an individual plane-line measurement $(\mathbf{\Pi}_i, \mathbf{l}'_i)$. All line candidates, both the correct and the incorrect, will be used as input to the RANSAC estimator described in the next subsection.

5.2 RANSAC

Wrong line detections are automatically removed with the RANSAC robust estimator. This algorithm iteratively generates different candidate solutions $(\mathsf{R}, \mathbf{t}, \mathsf{S})$ using the minimal solution with 4 random plane-line correspondences. Each candidate solution is evaluated by a cost function against the remaining $N-4$ plane-line measurements. In each iteration the best solution is updated whenever a candidate solution is found with the lowest cost function. After a certain number of iterations RANSAC stops and outputs the current best model.

Consider $N > 4$ measurements of planes $\mathbf{\Pi}_i$ and lines $\mathbf{l}'_i$ defined by their start and end points $\mathbf{w}'_i$, $\mathbf{z}'_{i,j}$. Each acquisition is represented by a vector $\mathbf{v}_{i,j} = \left(\mathbf{w'}^{\mathsf{T}}_{i,j}\ \mathbf{z'}^{\mathsf{T}}_{i,j}\ \mathbf{\Pi}_i^{\mathsf{T}}\right)^{\mathsf{T}}$. Some vectors $\mathbf{v}_i$ result from erroneous measurements and thus are outliers. The cost function to be minimized is the number of outliers, which are the measurements $\mathbf{v}_i$ whose residue r_j to the solution exceedes a pre-defined threshold t.

We now explain how to compute the residue r_i, given a measurement $\mathbf{v}_i$ and a candidate model $(\mathsf{R}, \mathbf{t}, \mathsf{S})$. The phantom plane $\mathbf{\Pi}'_i$ in the US reference frame is given by

$$\mathbf{\Pi}'_i = \begin{pmatrix} \mathsf{R}^{\mathsf{T}} & 0 \\ \mathbf{t}^{\mathsf{T}} & 1 \end{pmatrix} \mathbf{\Pi}_i \tag{15}$$

This plane can be projected onto the scan image as the 2D line

$$\tilde{\mathbf{l}}'_i = \begin{pmatrix} a_x^{-1} & 0 & 0 & 0 \\ 0 & a_y^{-1} & 0 & 0 \\ 0 & 0 & 0 & 1 \end{pmatrix} \mathbf{\Pi}'_i \tag{16}$$

which should be very close to the detected line $\mathbf{l}'_i$ for an inlier measurement and significantly misplaced for an outlier measurement. The residue r_i is the squared sum of the orthogonal distances between points $\mathbf{w}'_{i,j}$, $\mathbf{z}'_{i,j}$ and the 2D line re-projection $\tilde{\mathbf{l}}'_i$ of the calibration plane Π_i onto the image (Fig. 7(b))

$$r_{i,j} = ||\Delta \mathbf{z}'_{i,j}||^2 + ||\Delta \mathbf{w}'_{i,j}||^2 \tag{17}$$

5.3 Final Refinement

A final refinement of the calibration solution is performed using Levenberg-Marquadt iterative optimization [19]. After removing outliers with RANSAC, we convert each line segment $\mathbf{l}'_i$ into a discrete set of image points $\mathbf{p}'_{i,j}$ corresponding to each line pixel. We also reproject each plane $\mathbf{\Pi}$ onto the US image by representing it in the US reference frame and intersecting it with the plane $z = 0$. We minimize the total squared orthogonal distance between points $\mathbf{p}_{i,j}$ and the re-projected lines $\tilde{\mathbf{l}}_i$ in pixels (Fig. 7(b)).

6 Experiments and Results

This section reports experiments that validate and assess the accuracy of the proposed algorithm. All experiments are carried using a TITAN SONOSITE US system with a 2 - 4 Mhz curvilinear transducer that provides images with a resolution of 640×480. The pose of the US probe is estimated by attaching a planar


(a) Single-plane phantom

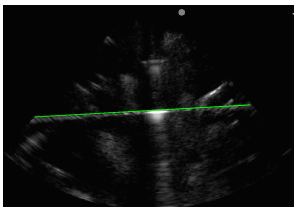
(b) Single-plane scan

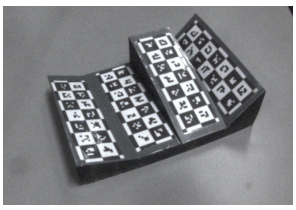
(c) Multi-plane phantom

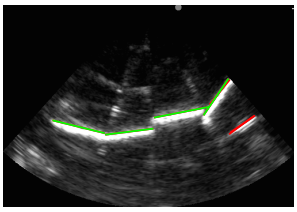
(d) Multi-plane scan

Fig. 8 Experimental acquisition

checkerboard pattern to the transducer that is visually tracked using a Grasshopper2 camera from PointGrey. Camera and pattern play, respectively, the roles of "stationary station" and "sensor/marker" (Fig. 1). All experiments are carried in a water tank with the plane phantom placed at the bottom. The phantom has also a visual marker attached that enables to determine its pose in camera coordinates before filling the tank with water.

Section 6.1 reports a first set of experiments in which the freehand 3D US is calibrated using a single plane (Fig. 8(a), Fig. 8(b)). It is shown that the propose algorithm provides accurate, repeatable results comparing favourably against the state-of-the-art. Section **??** describes a second experiment in which the single plane is replaced by a multi-plane phantom similar to the one used by Najafi et. al. [21] for obtaining more plane-line correspondences with fewer acquisitions (Fig. 8(c), Fig. 8(d)). The objective is to evaluate till which extent the proposed algorithm can be combined with this new phantom to further improve usability without sacrificing accuracy and robustness.

6.1 Single Plane

We acquired 30 scans of the single plane phantom for the purpose of testing the calibration algorithm. The line segmentation was carried in a fully automatic manner, as described in section 5.1, which may lead to some erroneous detections (outliers). A quick visual inspection of the detection results revealed that, from the 30 acquisitions, 21 lines seemed to be well estimated and 9 were clearly off. The 30 lines detections, including inliers and outliers, were used as input to the algorithm

Table 1 PRA for points at varying depths.

	0 – 40 mm	40 –80 mm	80 –120 mm	Total
10 images	2.27 ± 2.02	1.99 ± 2.02	2.35 ± 1.87	2.20 ± 1.97
20 images	1.17 ± 0.66	1.20 ± 0.80	1.42 ± 0.66	1.26 ± 0.72
30 images	0.92 ± 0.47	0.99 ± 0.65	1.25 ± 0.37	1.06 ± 0.53

leaving to RANSAC the task of automatically filtering the data (section 5.2).

The US probe was calibrated using an increasing number of frames ranging from $N = 10$ to 30. For each N we performed 50 trials using N randomly selected images out of the available 30. The distribution of rotation, translation, and scale parameters is displayed in 9. Both rotation and translation are decomposed into x, y, z components. The z-axis is perpendicular to the US measuring plane $\mathbf{\Sigma}$, while x and y axes are aligned respectively with the horizontal and vertical directions of the US scans.

The overall impression is that results are highly repeatable, which proves the robustness and reliability of the approach. As expected, variation tends to decrease with an increasing number N of input frames. It can also be observed that calibration results have a higher variation along the z-axis in translation and the x-axis in rotation. This is a known, persistent problem in US calibration [4,22] that is due to the fact that moderate changes in pose along these directions only produce very slight changes in US scan line measurements.

The accuracy of the calibration was then evaluated with the help of a 403 GS LE phantom (Fig. 10(a)). This phantom contains a set of precision-made parallel wires immersed in a tissue mimicking gel. The wires were located in the reference frame of the stationary tracking station (the camera reference frame) using a visual marker. The calibrated probe was directed towards the set of wires and the corresponding white blobs in the image were manually selected (Fig. 10(b)). For each scan we selected six points at depths ranging between 20 and 120 mm. These points were then reconstructed in 3D using each one of the 550 calibration trials depicted in Fig. 9. Note that in the phantom's gel, the sound travels approximately 3% faster than in water, which means that the scaling parameters a_x, a_y had to be adjusted by the same factor. The point re-construction accuracy (PRA) was finally computed as the distance between the reconstructed points and the known position of the wires along the US measuring plane.

The PRA distribution for all trials is displayed in Fig. 11(a). We also re-project the known wires on the US scan and measure their distance in pixels to the manually marked points (re- projection error, Fig. 11(b)). The results converge to a stable accuracy level of ap-

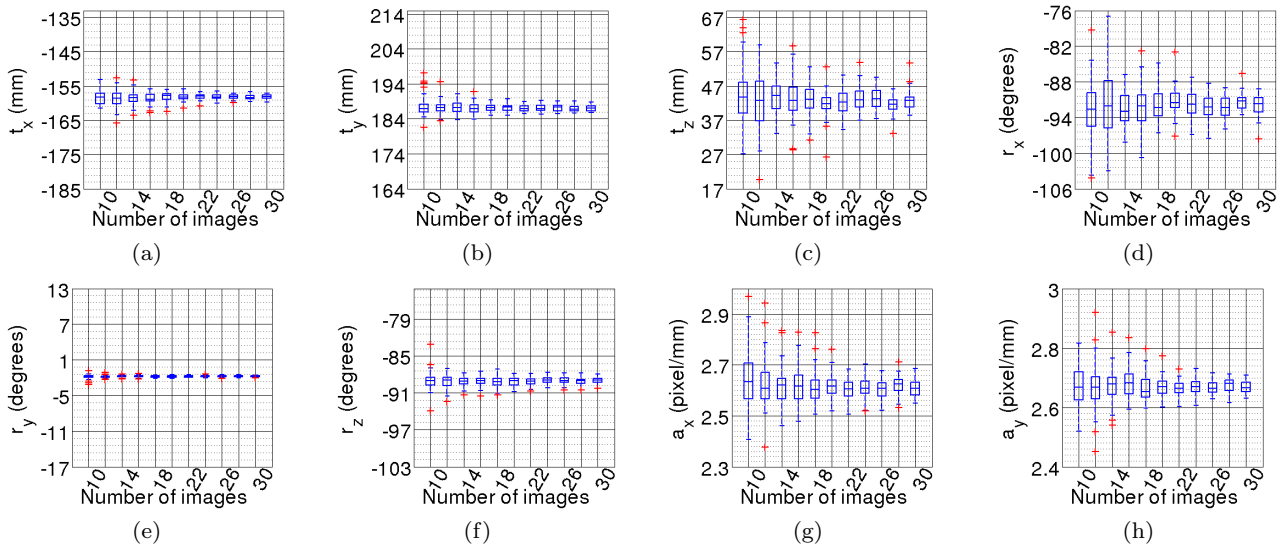

Fig. 9 Parameter distribution of 50 calibration trials for an increasing number of input images. The central blue markers represents median values, the blue box boundaries represent the lower and upper quartiles, and the red markers represent outliers.

Fig. 10 403 GS LE wire-phantom.

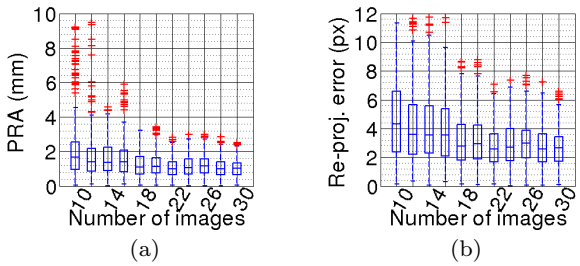

Fig. 11 Validation on 403 GS LE phantom. The central blue markers represents median values, the blue box boundaries represent the lower and upper quartiles, and the red markers represent outliers.

proximately 1 mm / 3 pixels for 22 or more images. Note that wire measurements in are detected as white elongated blobs occupying several pixels that are difficult to detect with a very high pixel accuracy. In Table 1 we display the PRA results with 10, 20, and 30 images for different depth ranges. The results are generally better for points with depths between 0 and 80 mm. This is to be expected, as the wire detection degrades with increasing depth (Fig. 10(b)).

Najafi et al. show in [22] that, for the same number of input frames, plane-based calibration achieves the same accuracy as competing methods with the advantage of using a much simpler phantom object. For 50 input frames and a maximum scanning depth of 50mm using a curvilinear transducer they report a PRA of about 1.00 mm. Table 1 shows that the method herein described reaches a similar accuracy with 30 frames. Moreover there are two important differences: First, our maximum scanning depth is 130 mm, which means that for depths up to 50mm the algorithm accomplishes an accuracy similar to [22] not only with less frames, but also using US scans with less than half the resolution. Second, while in [22] the line detection is supervised, in here the calibration process is fully automatic. Thus, the 30 frames include a significant number of outlier detections that are efficiently discarded by RANSAC without requiring time consuming verification by an experienced user.

7 Conclusion

We propose a minimal solution to the single-plane US calibration problem. Minimal solutions have been successfully used in many calibration problems from Computer Vision and in this paper we show that this methodology is useful to improve the state-of-the-art in planar phantom calibration, by achieving the same level of accuracy as previous approaches with less image acquisitions. Our method also provides a framework to handle

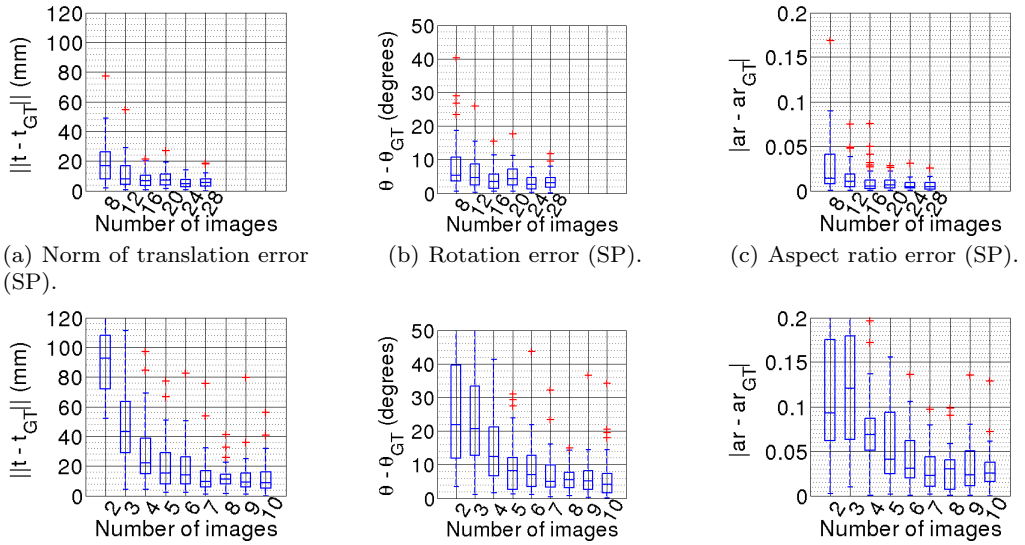

(a) Norm of translation error (SP). (b) Rotation error (SP). (c) Aspect ratio error (SP).

(d) Norm of translation error (MP). (e) Rotation error (MP). (f) Aspect ratio error (MP).

Fig. 12 Error distribution of 50 calibration trials with single plane (SP) and multi-plane (MP) for a growing number of images. The error is computed against a calibration with 30 images that is used as ground truth. The central blue markers represents median values, the blue box boundaries represent the lower and upper quartiles, and the red markers represent outliers.

fully automatic segmentation of the phantom in the US images. This approach simplifies the calibration procedure from the user perspective, by shortening its duration and eliminating the need for human supervision of the acquired data.

Acknowledgements The authors want to thank "QREN Mais Centro" by generous funding through grant "Novas Tecnologias para apoio á Saúde e Qualidade de Vida: Projeto A - Cirurgia e Diagnóstico Assistido por Computador Usando Imagem". Francisco Vasconcelos also acknowledges the Portuguese Science Foundation (FCT) that supported his work through grant SFRH/BD/72323/2010.

References

1. Ahmad, A., Orhan, S.O., Yildirim, M.C., Bebek, O.: Development and 3d spatial calibration of a parallel robot for percutaneous needle procedures with 2d ultrasound guidance. Journal of Medical Robotics Research **2**(04), 1750007 (2017)
2. Barratt, D.C., Penney, G.P., Chan, C.S.K., Slomczykowski, M., Carter, T.J., Edwards, P.J., Hawkes, D.J.: Self-calibrating 3d-ultrasound-based bone registration for minimally invasive orthopedic surgery. Medical Imaging, IEEE Transactions on **25**(3), 312–323 (2006)
3. Boctor, E.M., Iordachita, I., Fichtinger, G., Hager, G.D.: Ultrasound self-calibration. In: Medical Imaging 2006: Visualization, Image-Guided Procedures, and Display, vol. 6141, p. 61412N. International Society for Optics and Photonics (2006)
4. Chen, T.K., Thurston, A.D., Ellis, R.E., Abolmaesumi, P.: A real-time freehand ultrasound calibration system with automatic accuracy feedback and control. Ultrasound in Medicine & Biology **35**(1), 79 – 93 (2009). DOI http://dx.doi.org/10.1016/j.ultrasmedbio.2008.07.004
5. Duda, R.O., Hart, P.E.: Use of the hough transformation to detect lines and curves in pictures. Commun. ACM **15**(1), 11–15 (1972). DOI 10.1145/361237.361242
6. Fenster, A., Downey, D.B., Cardinal, H.N.: Three-dimensional ultrasound imaging. Physics in Medicine and Biology **46**(5), R67 (2001)
7. Fischler, M.A., Bolles, R.C.: Random sample consensus: A paradigm for model fitting with applications to image analysis and automated cartography. Communications of the ACM **24**(6), 381–395 (1981)
8. Gee, A.H., Treece, G.M., Prager, R.W., Cash, C.J.C., Berman, L.: Rapid registration for wide field of view freehand three-dimensional ultrasound. Medical Imaging, IEEE Transactions on **22**(11), 1344–1357 (2003). DOI 10.1109/TMI.2003.819279
9. Haralick, R.M., Lee, C., Ottenberg, K., Nölle, M.: Review and analysis of solutions of the three point perspective pose estimation problem. International Journal of Computer Vision **13**, 331–356 (1994). DOI 10.1007/BF02028352
10. Horn, B., Hilden, H.M., Negahdaripour, S.: Closed-form solution of absolute orientation using orthonormal matrices. Journal of the Optical Society of America A **5**(7), 1127–1135 (1988). DOI 10.1364/JOSAA.5.001127
11. Hsu, P., Prager, R.W., Gee, A.H., Treece, G.M.: Rapid, easy and reliable calibration for freehand 3d ultrasound. Ultrasound in Medicine & Biology **32**(6), 823 – 835 (2006). DOI http://dx.doi.org/10.1016/j.ultrasmedbio.2006.02.1427
12. Hsu, P., Prager, R.W., Gee, A.H., Treece, G.M.: Freehand 3d ultrasound calibration: A review. In: C. Sensen, B. Hallgrímsson (eds.) Advanced Imaging in Biology and Medicine, pp. 47–84. Springer Berlin Heidelberg (2009)

13. Isack H.and Boykov, Y.: Energy-based geometric multi-model fitting. International Journal of Computer Vision **97**(2), 123–147 (2012). DOI 10.1007/s11263-011-0474-7
14. Kindratenko, V.: A survey of electromagnetic position tracker calibration techniques. Virtual Reality **5**(3), 169–182 (2000). DOI 10.1007/BF01409422
15. Krupa, A.: Automatic calibration of a robotized 3d ultrasound imaging system by visual servoing. In: Robotics and Automation, 2006. ICRA 2006. Proceedings 2006 IEEE International Conference on, pp. 4136–4141 (2006). DOI 10.1109/ROBOT.2006.1642338
16. Kukelova, Z., Bujnak, M., Pajdla, T.: Automatic generator of minimal problem solvers. In: D. Forsyth, P. Torr, A. Zisserman (eds.) Computer Vision ECCV 2008, *Lecture Notes in Computer Science*, vol. 5304, pp. 302–315. Springer Berlin Heidelberg (2008)
17. Langø, T.: Ultrasound guided surgery: image processing and navigation. Ph.D. thesis, Fakultet for informasjonsteknologi (2000)
18. Lindseth, F., Langø, T., Bang, J., Hernes, N., Toril, A.: Accuracy evaluation of a 3d ultrasound-based neuronavigation system. Computer Aided Surgery **7**(4), 197–222 (2002)
19. Marquardt, D.W.: An algorithm for least-squares estimation of nonlinear parameters. SIAM Journal on Applied Mathematics **11**(2), 431–441 (1963)
20. Mercier, L., Langø, T., Lindseth, F., Collins, L.D.: A review of calibration techniques for freehand 3-d ultrasound systems. Ultrasound in Medicine & Biology **31**(2), 143 – 165 (2005). DOI http://dx.doi.org/10.1016/j.ultrasmedbio.2004.11.001
21. Najafi, M., Afsham, N., Abolmaesumi, P., Rohling, R.: A closed-form differential formulation for ultrasound spatial calibration: Multi-wedge phantom. Ultrasound in Medicine & Biology **40**(9), 2231 – 2243 (2014). DOI http://dx.doi.org/10.1016/j.ultrasmedbio.2014.03.006
22. Najafi, M., Afsham, N., Abolmaesumi, P., Rohling, R.: A closed-form differential formulation for ultrasound spatial calibration: Single wall phantom. Ultrasound in Medicine & Biology **41**(4), 1079 – 1094 (2015). DOI http://dx.doi.org/10.1016/j.ultrasmedbio.2014.11.020
23. Nistér, D.: An efficient solution to the five-point relative pose problem. IEEE Transactions on Pattern Analysis and Machine Intelligence **26**, 756–777 (2004). DOI 10.1109/TPAMI.2004.17
24. Prager, R., Rohling, R., Gee, A., Berman, L.: Rapid calibration for 3-d freehand ultrasound. Ultrasound in Medicine & Biology **24**(6), 855 – 869 (1998). DOI http://dx.doi.org/10.1016/S0301-5629(98)00044-1
25. Rousseau, F., Hellier, P., Barillot, C.: Confhusius: A robust and fully automatic calibration method for 3d freehand ultrasound. Medical image analysis **9**(1), 25–38 (2005)
26. Stewénius, H., Nistér, D., Oskarsson, M., Åström, K.: Solutions to generalized relative pose problems. In: Workshop on Omnidirectional Vision. Beijing China (2005)
27. Stolka, P.J., Foroughi, P., Rendina, M., Weiss, C.R., Hager, G.D., Boctor, E.M.: Needle guidance using handheld stereo vision and projection for ultrasound-based interventions. In: P. Golland, N. Hata, C. Barillot, J. Hornegger, R. Howe (eds.) Medical Image Computing and Computer-Assisted Intervention – MICCAI 2014, *Lecture Notes in Computer Science*, vol. 8674, pp. 684–691. Springer International Publishing (2014)
28. Talib, H., Peterhans, M., García, J., Styner, M., González Ballester, M.: Information filtering for ultrasound-based real-time registration. Biomedical Engineering, IEEE Transactions on **58**(3), 531–540 (2011). DOI 10.1109/TBME.2010.2063703
29. Toews, M., Wells, W.M.: Phantomless auto-calibration and online calibration assessment for a tracked freehand 2-d ultrasound probe. IEEE transactions on medical imaging **37**(1), 262–272 (2018)
30. Vasconcelos, F., Barreto, J., Nunes, U.: A minimal solution for the extrinsic calibration of a camera and a laser-rangefinder. Pattern Analysis and Machine Intelligence, IEEE Transactions on **PP**(99), 1 (2012). DOI 10.1109/TPAMI.2012.18
31. Vasconcelos, F., Peebles, D., Ourselin, S., Stoyanov, D.: Similarity registration problems for 2d/3d ultrasound calibration. In: European Conference on Computer Vision, pp. 171–187. Springer (2016)
32. Vitrani, M.A., Morel, G.: Hand-eye self-calibration of an ultrasound image-based robotic system. In: Intelligent Robots and Systems, 2008. IROS 2008. IEEE/RSJ International Conference on, pp. 1179–1185 (2008). DOI 10.1109/IROS.2008.4651013
33. Welch, J., Johnson, J., Bax, M., Badr, R., Shahidi, R.: A real-time freehand 3d ultrasound system for image-guided surgery. In: Ultrasonics Symposium, 2000 IEEE, vol. 2, pp. 1601–1604 vol.2 (2000). DOI 10.1109/ULTSYM.2000.921630
34. Zhang, H., Banovac, F., White, A., Cleary, K.: Freehand 3d ultrasound calibration using an electromagnetically tracked needle. In: Medical Imaging, pp. 61412M–61412M. International Society for Optics and Photonics (2006)